Mid-infrared spectroscopy of starbursts : from Spitzer-IRS to JWST-MIRI

Martínez-Galarza, J.F.

CHAPTER 5

Mid-infrared IFU spectroscopy from space: wavelength calibration of JWST-MIRI[1]

In 2018 a new integral field unit (IFU) spectrometer will fly to space onboard the *James Webb Space Telescope* (JWST), as one of the components of its *Mid-Infrared Instrument* (MIRI). With an approximate wavelength coverage from 5 μm to 29 μm and a field of view ranging from $3.7'' \times 3.7''$ to $7.9'' \times 7.9''$ depending on the wavelength, this medium resolution spectrometer (MRS) will study the infrared sky at spatial scales 10 times smaller, sensitivities 100 times larger and spectral resolution 5 times better than its natural predecessor, the *Infrared Spectrograph* (IRS) onboard the *Spitzer Space Telescope*. In this chapter we present a method for the ground wavelength calibration of the MRS. We test our method using data collected during testing of the Verification Model (VM) of the instrument, and obtain a first calibration of one of the spectrometer sub-channels. We compare our results with predictions from optical models and combine them with a study of the fringing pattern created within the detector substrate, to verify some of the spectroscopy requirements set by JWST's science goals. We demonstrate the reliability of our method and show compliance with the spectral resolution requirements for the studied sub-channel. In Chapter 6 we apply our method the the full wavelength range of the Flight Model of the instrument.

[1] Partially based on: J.R. Martínez-Galarza, A. M. Glauser, A. Hernán-Caballero, R. Azzollini, A. Glasse, S. Kendrew, B. Brandl and F. Lahuis, 2010, SPIE Proceedings, San Diego.

5.1 Introduction

The powerful capabilities of the *James Webb Space Telescope* (JWST) at mid-infrared wavelengths (5 μm-29 μm) have been widely recognized by the astronomical community. Practically all of the JWST science themes will greatly benefit from observations extending into the thermal infrared. For example, at redshifts where the first light sources in the history of the Universe are expected to form ($z > 8$), several spectral features from evolved stellar populations have shifted into wavelengths beyond the JWST near infrared instruments, making it necessary to observe at MIR wavelengths to distinguish between real "first light" sources and sources with older stellar populations. Before JWST, observations in this spectral range have been limited to apertures below 1 meter, and to spectral resolving powers of $R \sim 600$, both limits imposed by the capabilities of the *Spitzer Space Telescope*. As we have have pointed out in Chapter 1, the larger aperture size of JWST (6.5 m) implies a sensitivity 100 times larger than Spitzer in the wavelength range 5 μm-10 μm.

As the only mid-infrared instrument onboard the JWST, MIRI will provide multiple configurations that include wide-field imaging and photometry, coronagraphy between 10 μm and 27 μm, low-resolution (R$\sim$ 100) slit spectroscopy between 5 μm and 10 μm and medium resolution integral field spectroscopy with a velocity resolution of $\sim$ 100 km s^{-1} ($R = 1000 - 3000$) between 5 μm and 28.5 μm. The instrumental requirements for all these capabilities are set by the science goals of the mission and can be separated into two main aspects: diffraction limited image quality and high sensitivity. With a main aperture of 6.5 m, JWST has diffraction limits at 10 μm and 20 μm of 0$''$.317 and 0$''$.645 respectively, with a pixel size on the MIRI detectors of 0$''$.11. This guarantees a fully sampled diffraction limit for $\lambda > 7$ μm, which has not been achieved by previous observatories at the same wavelengths. As for the sensitivity, the goal is to ensure that the noise level is set by the thermal infrared background from cosmic sources, and the telescope itself. This requires high photon conversion efficiency and, of particular relevance for the present chapter, spectral and spatial resolutions that match the potential scientific targets.

The sensitivity requirements can only be achieved with an instrument that operates at very low temperatures, an hence MIRI is the only one of the JWST instruments that is cooled to a temperature of 7 K, considerably lower than the 40 K operational temperature of the telescope. The MIRI cooler is hybrid, and uses a Joule-Thomson adiabatic cooler precooled by a multi-stage Pulse Tube Cooler (Banks et al. 2008). This configuration allows remote cooling, which is necessary to place the instrument far from the warm parts of the cooling system. Because of this low-temperature operation, MIRI has to be tested in a cryochamber that simulates the operational conditions.

In this chapter we present spectral data obtained during testing of the Verification Model (VM) of the instrument, an almost exact copy of the instrument that will actually fly with JWST in 2018. We design a method to perform the wavelength calibration of the MRS, and apply it to the test data for one of the instrument sub-bands. We derive a wavelength range and spectral resolution for this sub-band, and compare them with predictions from optical models of the instrument. We demonstrate that our method is reliable and able to provide wavelength calibration within the required uncertainties, even

within the limitations of the VM hardware. The method provides us with a powerful tool to measure the wavelength calibration of the MRS across the full wavelength-range, once the Flight Model (FM) becomes available. We perform the full wavelength calibration in Chapter 6.

The chapter is structured as follows. In §5.2 we introduce the medium resolution spectrometer (MRS), and indicate some generalities of its functionality. In §5.3 we describe the spectrometer setup during VM testing, and present the resulting measurements. Since the wavelength calibration is tightly related to the spatial information of the IFU, we start §5.4 with a description of the algorithms for the reconstruction of the datacubes. We also describe the method used to perform wavelength calibration, and its application to channel 1C. Finally, we discuss fringing, resolving power and the instrumental line shape. We summarize our results in §5.5.

5.2 MIRI: an overview

5.2.1 The MIRI field of view on the sky

The field of view of MIRI on the sky is divided in different regions, each dedicated to one of the instrument functionalities. It has a $75'' \times 113''$ field of view for the imager, a $30'' \times 30''$ field of view with a Lyot coronagraph that operates at 23 μm, three 4-Quadrant Phase Mask Coronagraphs, each with a field of view of $24'' \times 24''$ and operating at 10.7 μm, 11.4 μm, and 15.5 μm, a $5'' \times 0''.6$ slit for low resolution spectroscopy and four nested fields of view for the IFU spectrometer. These are offset from the field of view containing the imager, coronagraphs and low resolution slit, as we show in Fig. 5.1. We also show in Fig. 5.1 how the focal plane looks like on the three MIRI detectors.

5.2.2 Integral field spectroscopy with MIRI

The MRS is composed of two main optical components. The spectrometer pre-optics (SPO) (Wells et al. 2004) separate the incoming beam in 4 spectral channels by the use of dichroics, and divide the field of view of each channel using slicing mirrors. The spectrometer main-optics (SMO) (Kroes et al. 2010), consist of three sets of diffraction grating mechanisms that divide each MRS channel in three sub-bands (short, medium and long wavelengths) and record the resulting spectrum on two MRS detectors (Ressler et al. 2008). In Table 5.1 we list all the nominal sub-bands of the MRS, with their respective nominal wavelength ranges and the number of MRS slices.

Each of the two MRS detectors registers the dispersed spectrum of two channels simultaneously. In Fig. 5.2 we show schematically how a particular field of view is divided by the slicing mirrors for each channel and, and then dispersed into the detector. In Table 5.2 we provide some relevant numbers regarding the size of the FOV and the spatial sampling for each channel.

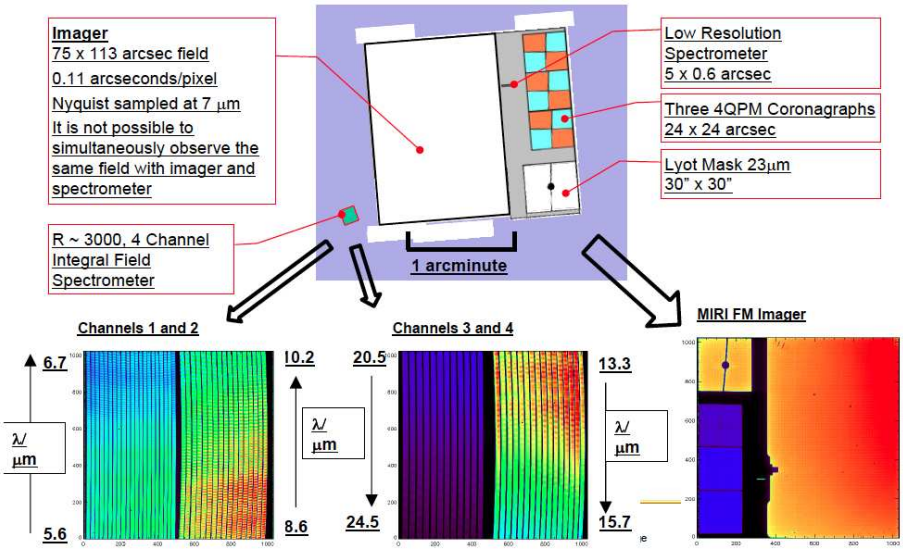

Figure 5.1 The MIRI FOV on the sky and on the detectors. The sizes of the different fields of view is indicated. Courtesy of the MIRI European Consortium.

For the MRS, specific requirements to accomplish the proposed science include a field of view of at least 3 arcseconds and the capability of image reconstruction within 10% of the diffraction limit. On the spectral side, the MRS is required to have a resolving power $R > 2400$ for 5 μm $< \lambda <$ 10 μm, $R > 1600$ for 10 μm $< \lambda <$ 15 μm and $R > 800$ for 15 μm $< \lambda <$ 27 μm, and the wavelength determination accuracy should be of 10% the size of the resolution element at all wavelengths. Also, spectral ghosts are expected to be of less than 1% measured as the brightness of an unresolved line fitted to a ghost image relative to the brightness of the primary line. Finally, wavelength stability is expected to the level of 5% of the resolution element size.

5.3 Setup and measurements

5.3.1 The MIRI Telescope Simulator (MTS)

To provide the Verification Model with an input signal, a MIRI Telescope Simulator (MTS) (Belenguer et al. 2008) has been developed by INTA. Its main purpose is to provide a test beam for MIRI similar to the one that will be delivered by JWST under flight conditions. Light from a 800 K blackbody is collimated and passed through a variable aperture system and then trough the desired filter before a diffuser spreads the beam and makes the illumination uniform. A 100 μm pinhole on the extended source target provides

Subchannel	Wavelength Range μm	No. of Slices	FOV arcsec^2
1A	4.87-5.82	21	3.7×3.7
1B	5.62-6.73	21	3.7×3.7
1C	6.49-7.76	21	3.7×3.7
2A	7.45-8.90	17	4.5×4.7
2B	8.61-10.28	17	4.5×4.7
2C	9.94-11.87	17	4.5×4.7
3A	11.47-13.67	16	6.1×6.2
3B	13.25-15.80	16	6.1×6.2
3C	15.30-18.24	16	6.1×6.2
4A	17.54-21.10	12	7.9×7.7
4B	20.44-24.72	12	7.9×7.7
4C	23.84-28.82	12	7.9×7.7

Table 5.1 Nominal characteristics of the MRS subchannels

Channel	Across slice sampling [arcsec]	Along Slice sampling [arcsec]	Across slice Inst. FOV [arcsec]	Along Slice Inst. FOV [arcsec]
1	0.18	0.20	3.7 (21)	3.7
2	0.28	0.20	4.5 (17)	4.7
3	0.39	0.25	6.1 (16)	6.2
4	0.64	0.27	7.9 (12)	7.7

Table 5.2 The spatial sampling and instantaneous FOVs of all MRS channels. The third column indicates in parenthesis the number of slices in which the FOV is divided.

the point-source capabilities. This point source can be scanned across the MIRI FOV. An imaging subsystem then sends the light to the MIRI FOV through a set of focusing and folding mirrors.

The MTS was meant to project a point source onto the FOV of MIRI, as well as an extended uniform illumination. Due to some mechanical issues during the manufacturing of the MTS, it was not possible to properly focus the point source, and hence its Point Spread Function (PSF) was significantly distorted. Additional mechanical issues prevented us to illuminate the entire MIRI field of view with the extended source mode. Unfortunately, the non-illuminated area includes the FOVs of the four MRS channels. The MTS is also equipped with several narrow-band filters, etalons to provide synthetic spectral lines in the full range, and a mask to produce dark images. It also has two cutoff filters, a long wavelength pass (LWP) and a short wavelength pass (SWP) filter. The MTS etalons are Fabry-Perot interferometers that produce synthetic spectral lines at specific wavelengths by interference of two reflected wave fronts. The pattern of this etalon lines can be resolved by the MRS.

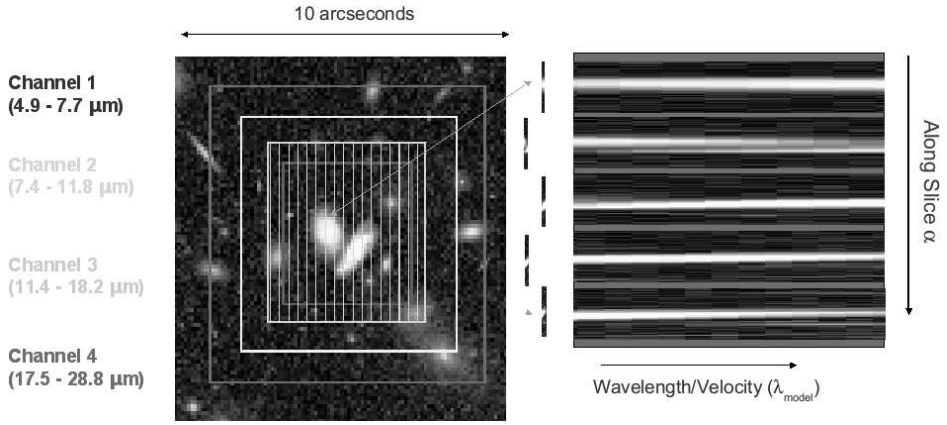

Figure 5.2 IFU spectroscopy. The slicing of the FOV is performed by the spectrometer pre-optics and arranged in an output format, for each of the four nested FOVs (left). Light is dispersed by first-order gratings and forms a spectrum on the detector (right).

5.3.2 Measurements

Using the setup described in the previous section we have taken MRS spectra of the etalon lines for the different available subchannels. Since full illumination of the MRS field of view was not possible, we used the out-of-focus point source to illuminate two regions of the MRS field of view. Full illumination of the MRS FOV will be possible during FM testing. For each of those etalon exposures we also took a background image by moving the point source out of the image field and taking an exposure of the same duration. Additionally, for each of the two point source positions we took exposures using the MTS LWP filter, and the 800 K blackbody continuum, without any filters. The LWP exposures are crucial to fulfil our goal, since the filter cutoff provides an absolute wavelength reference for the calibration. This cutoff wavelength falls within the range of channel 1C, and hence we use this channel for the present analysis.

The MIRI detectors have two standard readout patterns: Fast Mode and Slow Mode. Fast Mode reads the full array every 2.775 seconds, and Slow Mode performs the same operation every 27.105 seconds. The slow mode is preferred for long exposures ($>\sim 10$s), in order to reduce the data volume. The exposure parameters used in the present study are listed in Table 5.3.

Fig. 5.3 shows the resulting detector signal for channels 1C and 2C for an etalon exposure. The slices into which the FOV has been divided are arranged along the horizontal axis, while the vertical direction corresponds to the dispersion axis. Each of the vertical 'slices' on the detector plane is then the spectrum of one spatial slice of the FOV. The etalon lines are clearly visible as dots more or less equally spaced along the dispersion axis. They are not present in all the spatial slices, since not all the FOV was illuminated,

NFrames	40
NInt	1
Readout	SLOW
Int. Time	120 sec
VAS %	100

Table 5.3 Exposure parameters.

as mentioned. Optical distortions within the MRS are evident as a curvature of the spectrum. We expect these distortions to produce an observable variation in the position of equal-λ points as we move in the along-slice (spatial) directions.

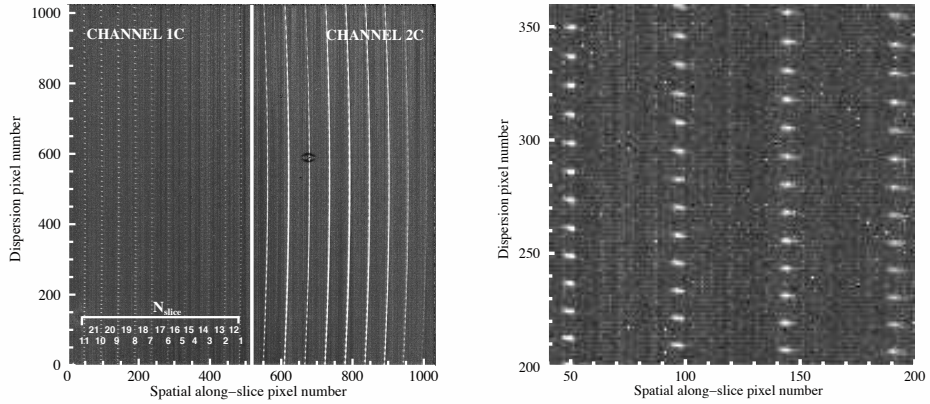

Figure 5.3 *Left:* An etalon exposure using the MRS for channels 1C and 2C. The horizontal axis corresponds to the spatial along-slice direction, while the vertical axis corresponds to the dispersion direction. The slice numbers are indicated. *Right:* Detail of the same etalon exposure. Etalon lines appear as little blobs aligned along the dispersion axis.

5.4 Analysis

5.4.1 Cube reconstruction

In an IFU spectrometer like the MRS, the spectral and spatial information are closely related, because the FOV of each channel is optically sliced, re-aligned, and then dispersed by the gratings to generate the image spectra of Figs. 6.3, 6.4 and 6.6. Hence, although the main focus of this and the following chapters is the wavelength calibration, a brief discussion on the datacube reconstruction algorithm is necessary before we describe the

analysis in detail. The algorithm builds the datacube from the flat-fielded slope image, and it has been implemented in the DHAS software. The resulting cube has two spatial dimensions, corresponding to sky coordinates, and a wavelength dimension.

In Fig. 5.4 we illustrate the basic concept of the cube reconstruction. The IFU level 3 data shows close-to-parallel stripes that correspond to the spectra of each of the slices in which the FOV is divided. The three dimensions of the cube are the along-slice direction, (α), the across-slice direction, β, and the wavelength direction, λ. Because of the optical distortions as the light traverses the spectrometer optics, this reconstruction is not straightforward.

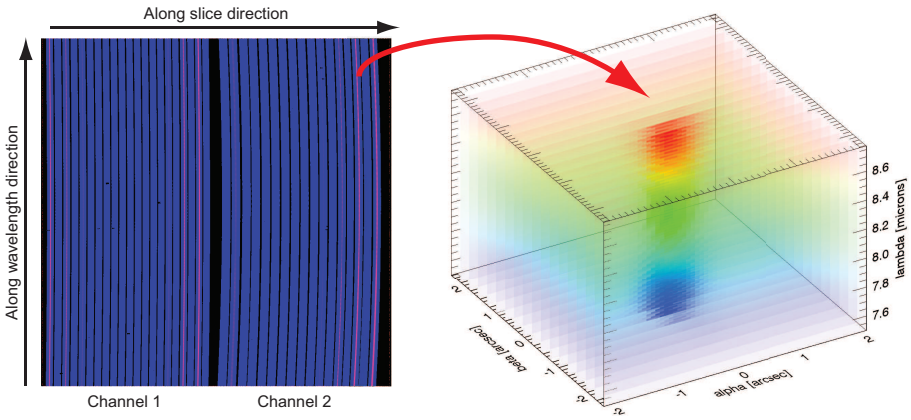

Figure 5.4 A schematic view of the cube reconstruction from raw IFU data. The two-dimensional information from the raw data (left) is transformed into the three-dimensional structure (right).

The earlier stage of the calibration is based on the optical models that trace the rays between the astronomical object in the sky plane and the positions on the detector, as a function of wavelength. Using these models, a map is produced between the corners of each of the 1024×1024 detector pixels (x, y), and the sky coordinates (α, β) and wavelength (λ). These maps are a first guide to rebin the detector pixels into the cube space.

These transformation maps also allow for global variations in the alignment of the slices between the optical model and the as-built instrument, that will result in variations of the α coordinate as a function of β. Using test images of the focal plane obtained during testing, it is possible to measure these offsets by determining the slice center in these images from the slice edges, and then compare them with the model predictions. Fig. 5.5 shows and explains the principle of this correction.

This method is not perfect, because it relies on the assumption of symmetric edges of the slices, an hence additional offsets of the observed α coordinate with respect to the models were observed during the testing. These additional offsets were corrected using the totality of the dataset to measure the spatial distortions, but this is outside the scope

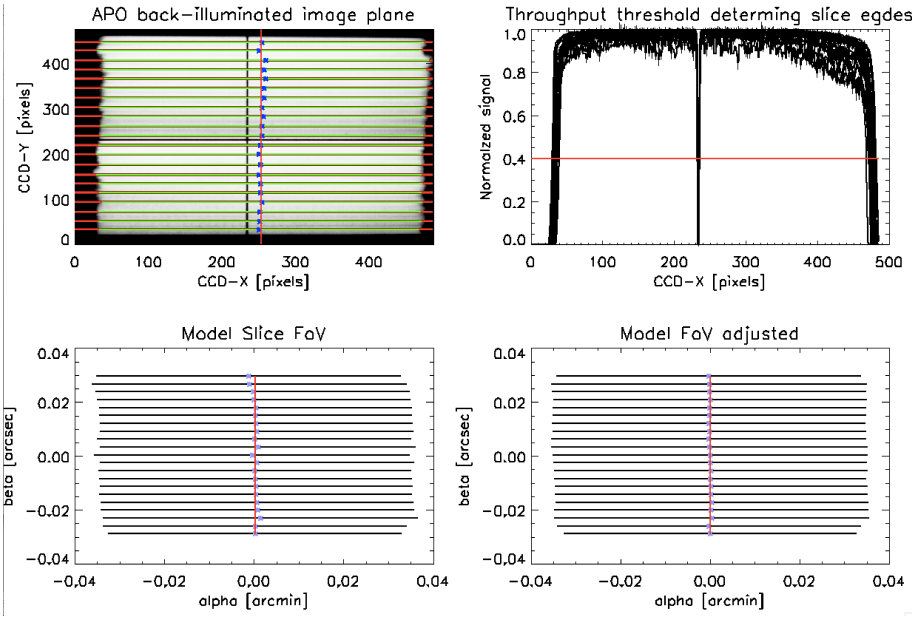

Figure 5.5 Correction of the slice-to-slice offsets of the α-coordinate: The top left panel shows the input plane of Channel 1. Along each red line the signal for each slice is extracted and normalized (right top panel). The centre of the slice (blue stars) is determined by using the relative signal strength (40%) as a discriminator for the slice. The slice centres are then compared with the slice centres of the optical model (bottom left panel) and adjusted correspondingly (bottom right).

of this chapter. Of relevance to us is that after the corrections, the resulting reconstructed PSFs were very stable all over the FOVs for all subchannels.

5.4.2 Etalon analysis

From the MRS exposures that we have described in the previous §5.3.2 we can reconstruct the image of the point source on the FOV at different wavelengths using the cube reconstruction algorithm, to obtain the 3D datacubes.

We start our analysis with the resulting datacubes, produced from from background-subtracted exposures. We use the following coordinate system for the data cube: α is the space coordinate in the along-slice direction, β is the space coordinate in the across-slice direction and $\lambda_{\rm model}$ is the wavelength. Both α and β are measured in arcseconds and are referred to the center of the FOV, while the wavelengths are in microns and their absolute value comes from the optical model. Here we will compare the optical model

wavelengths λ_{model} with the wavelengths resulting from our etalon and LWP measurements and analysis. We refer to the measured wavelengths as λ_{meas}, to differentiate them from the theoretical wavelengths.

The dimensions of the cube are 25 pixels in the α direction, 21 pixels in the β direction and 1225 wavelength bins. It is important to note that each of the 21 pixels in the across slice direction (β) is associated with one of the 21 slices shown in Fig. 5.3. The spatial sampling is 0.18 arcsecs in the α direction and 0.17 arcsecs in the β direction. This results in an effective FOV size of 4.48" $\times$ 3.56".

The left panel of Fig. 5.6 shows a layer of the data cube for a particular value of λ_{model}. The original exposure corresponds to a continuum 800 K blackbody exposure. The resulting image shows the point source near one of the corners of the FOV, with an elongated PSF due to the focusing problem of the MTS that we have mentioned before. The right panel of Fig. 5.6 shows a background exposure where we have indicated the pixels where we have measured the etalon lines with enough signal to noise to perform this analysis, and where we also have a good measurement of the continuum and filter spectra. These areas of the FOV correspond to two different pointings of the point source, and are intended to cover as many pixels as possible. We will use these well separated regions to study the variation of the wavelength properties and resolving power with position of the point source on the FOV.

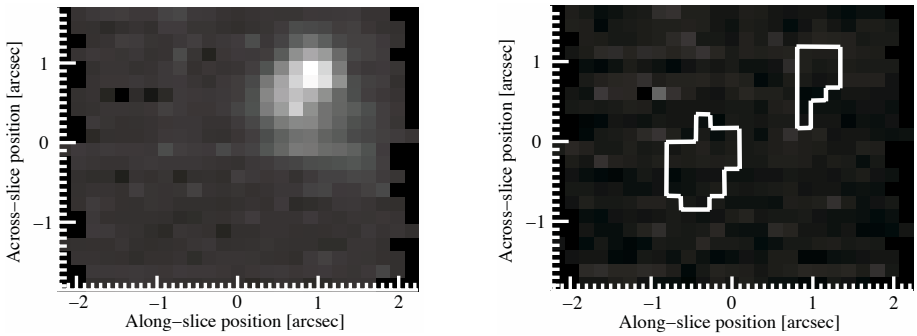

Figure 5.6 *Left*: The reconstructed point source at a particular wavelength. The elongated shape is due to focusing problems of the MTS. The horizontal axis corresponds to the along-slice spatial coordinate, α, while the vertical axis corresponds to the across-slice spatial coordinate, β. *Right*: The areas of the MRS field of view where enough signal to noise ratio was achieved for this analysis, and where LWP and continuum exposures were also taken.

The method works as follows: for each available (α,β) position we extract the spectrum of the etalon lines exposure and that of the LWP filter exposure. Provided that we know the wavelengths of the etalon lines, they provide a relative wavelength calibration along the full wavelength axis for channel 1C. On the other hand, the cutoff wavelength of the LWP spectrum provides an absolute wavelength reference for a single point in the

wavelength axis. We combine the information from this absolute reference with the relative information from the etalon lines to obtain a final wavelength scale. The uncertainty of our method depends on the accuracy with which we are able to identify the etalon line peak positions and the shape of the filter cutoff slope. This accuracy is of course a function of the signal-to-noise (S/N) ratio at which the spectra are detected. Other effects, such as line undersampling, also have to be taken into account.

The left panel of Fig. 5.7 shows a segment of the extracted etalon spectrum for ($\alpha = -0.269$ and $\beta = -0.170$). Lines are well detected with a S/N ratio of about 15, and the separation between them is well resolved, as expected for the MRS resolving power. The pixel sampling of the etalon line profiles adds an uncertainty to our determination of line peaks. Therefore, we fit Gaussian profiles to the lines in order to obtain a more accurate estimate of the peak position. We will discuss the shape of the line profile later in this paper.

The error in the line position associated with the Gaussian fit is of the order of 0.02 resolution elements. This is, as we will see later, below the instrument requirement for wavelength accuracy. However, the fact that the lines are undersampled and the presence of other sources of noise such as electronics, cosmic rays or bad pixels make the absolute determination of the line positions somewhat more uncertain than the error derived from the Gaussian fit. We expect these lines to be unresolved, and hence, while their centroid positions will provide us with a way to calibrate the wavelengths, their width will give us information about the resolving power of the instrument.

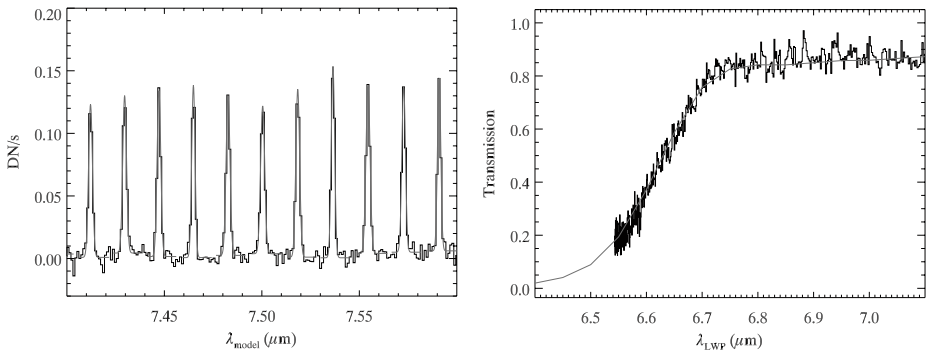

Figure 5.7 *Left*: The extracted etalon spectrum for a particular (α, β) value. Signal-to-noise ratio for the etalon lines is about 15. Lighter grey lines are Gaussian fits to the data, which is shown as a solid black line. *Right*: The transmission profile of the LWP filter. The lighter grey line is the calibrated curve, while the black line is the measured data. We fit the two curves to find an absolute reference in wavelength.

The peak positions of the etalon lines must be related to wavelengths obtained independently with high accuracy. For this purpose, we use a high resolution ($R \sim 10^5$) spectrum of the etalon transmission pattern measured independently at the Rutherford

Appleton Laboratory, in the United Kingdom. This measurement provides the relative wavelengths of the etalon lines with an accuracy of the order of 10 angstroms, i.e., far beyond our instrument requirement. Now we only need an absolute reference, and for that we use the cutoff slope of the LWP filter spectrum.

The right panel of Fig. 5.7 shows the LWP fit for a particular position in the FOV. The cutoff is clearly visible as a fading slope of the flux between 6.5 and 6.7μm. This spectrum is the product of the continuum emission from the 800 K source and the transmission curve of the filter. To obtain an uncalibrated transmission curve from our measurements, we divide the LWP spectrum obtained with the MRS by the 800 K continuum spectrum at the same (α, β) position. We fit the resulting curve to the previously measured filter profile that samples the transmission as a function of the calibrated wavelength $\lambda_{\rm LWP}$. It is important to note that this fit does not represent the final dispersion relation yet, but only a first order approximation to find the wavelength of a single bin. Higher orders are not so relevant at this stage, since the accuracy of the determination of the reference bin has to be lower than the separation between etalon lines only (about 0.014 μm at 6.6 μm).

In the final step we use the position of the etalon line centroids and the wavelength of the reference bin to create a grid of bin number vs. wavelength along the full range of channel 1C. We fit a second order dispersion relation to this grid and apply it to the full set of bins for each available (α,β) position. In this way we obtain a calibrated set of wavelengths for the cube bins which are illuminated. This wavelengths ($\lambda_{\rm meas}$) are independent from the theoretical wavelengths $\lambda_{\rm model}$.

Fig. 5.8 shows the difference between $\lambda_{\rm model}$ and $\lambda_{\rm meas}$ for different slice numbers, in units of the measured resolution element (see section 3.3). This difference increases linearly as we go to longer wavelengths, and there is a noticeable shift in the difference as we move from one slice to another. The vertical red line in the plot represents half the separation between etalon lines, and hence the minimum error we should expect from effects of line misidentification. The slice to slice variations we are observing are smaller than this minimum error, and hence must arise from different causes. The $\lambda_{\rm meas} - \lambda_{\rm model}$ difference spans a range of approximately 8 resolution elements for a given slice number, while the offset difference from one slice to another is about 0.2 resolution elements.

The difference plotted in Fig. 5.8 is a measure the deviations between the designed and the built spectrometer. For instance, the zero order effect is due to alignment offsets of the detectors or the gratings. The first order effect could be partially explained by a small tilt in the detector, while the second order effects are the result of differences in the optical distortion between the as-build and the as-designed instrument. Obviously, the uncertainty in the knowledge of the LWP cutoff also adds to this difference. The first order effect seems to dominate the difference in this wavelength range.

5.4.3 Fringing

The modulation in intensity along the dispersion axis known as fringing is a common feature in infrared spectrometers and is due to the interference of wavefronts reflected by different layers of the detector. Several de-fringing algorithms have been developed

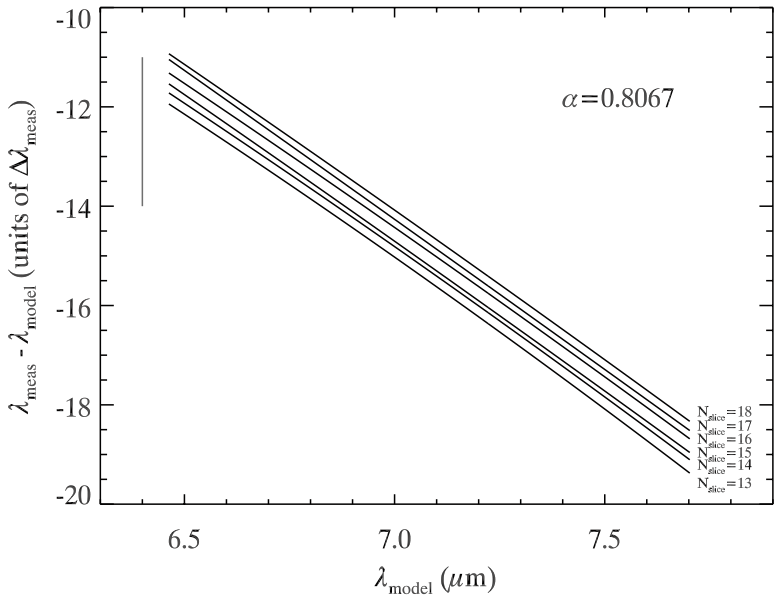

Figure 5.8 . Difference between modelled and measured wavelength for different slice numbers, for a particular along-slice position. The length of the vertical grey line is half the separation between etalon lines.

for infrared detectors of different characteristics. We can use the information contained in the fringing pattern in one of the following ways: either we use the wavelengths of the maxima and minima as compared to the predictions from the optical model to derive accurate detector features such as thickness, refractive index, etc., or we assume a model of the detector and use the distortions in the phase and period of the fringes to obtain a wavelength calibration of the instrument. Here we will attempt this latter option.

We assume that the detector has perfectly plane-parallel surfaces. Under this assumption, the period of the fringes should be constant in the wavenumber (k) domain, and deviations from this condition can be used to correct the wavelength. More specifically, if k is the *correct* wavenumber for each wavelength bin in the cube, then the frequency of the fringes is constant in k, and we should observe a linear increase of the phase ϕ with k, with proportionality factor ω:

$$\phi - \phi_0 = \omega(k - k_0) \tag{5.1}$$

We can use this relation to find the wavelength calibration for a particular spatial location in the detector:

$$k = k_0 + \frac{\phi - \phi_0}{\omega} \tag{5.2}$$

provided that k_0 and ω are known. From the assumed detector thickness we can obtain the separation between fringes ($k-k_0$), which corresponds to a phase difference of 2π, and hence we obtain ω. As for the absolute reference wavelength k_0, we find it again using the LWP filter cutoff wavelength. However, unlike the etalon analysis that uses relative differences between etalon lines, in this case the absolute calibration relies completely on the fit to the cutoff slope of the filter.

The fringes are obtained from VM exposures using the MIRI calibration source, which provides uniform illumination over the full FOV. Fig. 5.9 shows the resulting fringes for a particular value of α and β. A sinusoidal function is fitted to the baseline-corrected pattern and the position of the fringes maxima is compared with the predictions from the detector model, both in frequency and phase. Deviations are translated into wavelength difference with $\lambda_{\rm model}$, as described.

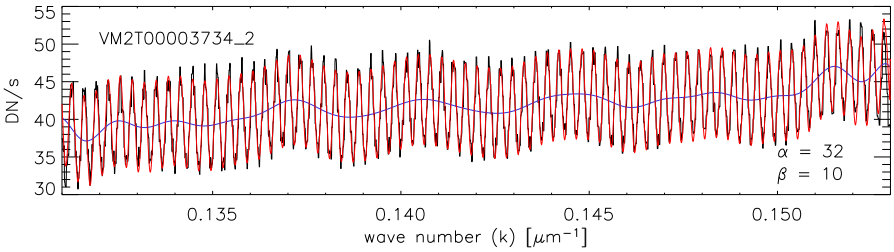

Figure 5.9 Measurement of the phase of the fringes. The black line represents the counts in the datacube as a function of wavenumber for a given α, β. The blue line is the low-frequency oscillation obtained through FFT filtering, and the red line is the cosine of the phase calculated for each k, cos(ϕ), after scaling to match the amplitude of the fringes and addition of the low-frequency oscillation. Here α and β refer to the spatial bin number and the slice number, respectively.

The left panel of Fig. 5.10 shows the correction in wavelengths with respect to $\lambda_{\rm model}$ derived using the fringes for all the 21 slices. The shape of the shift varies smoothly as a function of the slice number (i.e., as a function of the slice position on the detector plane). The U-shape of the shift for some of the slices might be due to variations in the detector thickness that are not accounted for in the detector model. But they could also be due to optical distortions in the MRS itself. This result needs to be corroborated during the etalon lines calibration, once the full FOV can be illuminated with the MTS extended source.

We compare the results obtained with the two methods for two different slices in the right panel of Fig. 5.10. This comparison is only relative, since the strong dependence of the fringing method on the absolute reference makes any absolute comparison meaningless. The difference is significant. The dependence with slice position is much more dramatic when the fringes are used. Also, second order effects seem to dominate the

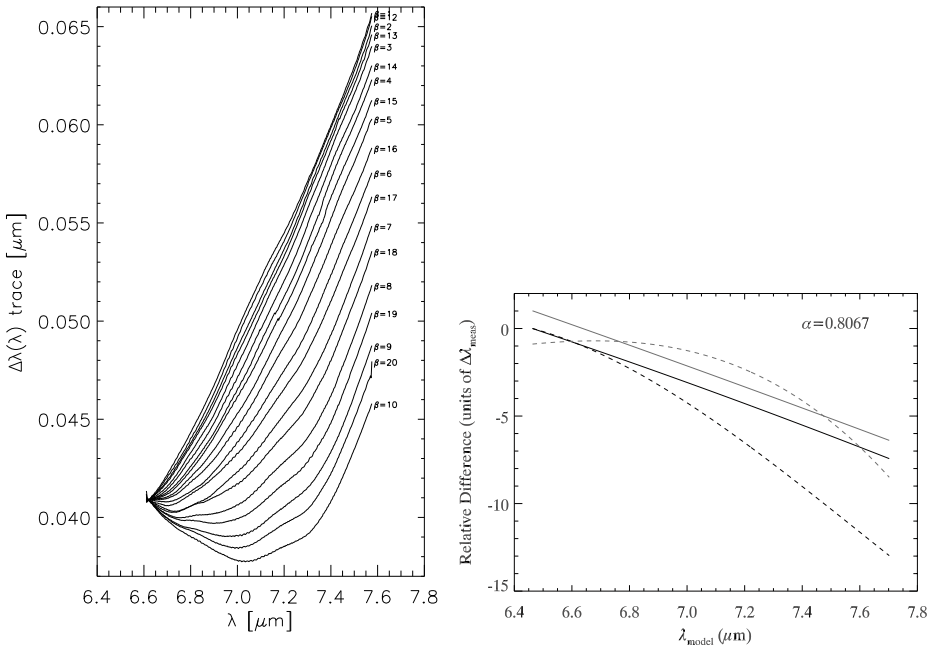

Figure 5.10 *Left*: Shift with respect to $\lambda_{\rm model}$ that needs to be applied to each slice as calculated using the fringing analysis. Here, β refers to the slice number. *Right*: Relative difference in the corrections to the model wavelengths when using the two methods described. Solid lines correspond to the etalon analysis, while dashed lines correspond to the fringing analysis. We compare two positions on the MRS FOV: $N_{\rm slice} = 13$ (black lines), and $N_{\rm slice} = 18$ (lighter grey lines). The origin of the *y* axis is arbitrary.

fringing analysis, while the difference with $\lambda_{\rm model}$ are close to linear with wavelength in the etalon analysis. The smooth variation in the shape of the curves shown in the left panel of Fig. 5.10 might be an indication that the difference between the two methods might arise from wrong assumptions about the detector properties. For instance, thickness variations (deviations from plane-parallel geometry) of the detector would produce additional distortions on the phase and frequency of the fringes. Whether this is the case, or there are other issues about the wavelength calibration that we are ignoring in the etalon analysis is a question that will have to wait until we have fully characterized FM detectors and better S/N data.

5.4.4 Line shape and resolving power

The etalon lines are not resolved by the MRS. This is shown in the left panel of Fig. 5.11, where we have plotted the high resolution measurement of one of the etalon lines together with the corresponding line as measured with the MRS during the tests. The width of the unresolved lines provides information about the resolving power of the instrument. We have determined the widths of the measured etalon lines by fitting Gaussians to the line profiles and using their full width at half maximum (FWHM). To associate the FWHM of the lines (in pixels) to the resolution element $\Delta\lambda$ (in μm), we use the derivative of the dispersion relation that we have obtained from the etalon analysis. We compute the resolution element at the positions of the lines and plot the result for a particular (α, β) in the right panel of Fig. 5.11, where we have also fitted a straight line to the set of datapoints. The linear fit gives a resolving power ($R = \lambda/\Delta\lambda$) between 2800 (at short wavelengths) and 3400 (at long wavelengths) for the derived wavelength range (6.43-7.66 μm). Deviations in R from the straight line are of about 500. The instrument requirement for resolving power states that between 5 and 10 μm, the resolving power should be greater than 2400. The goal, however, is to provide $R \sim 3000$ at these wavelengths.

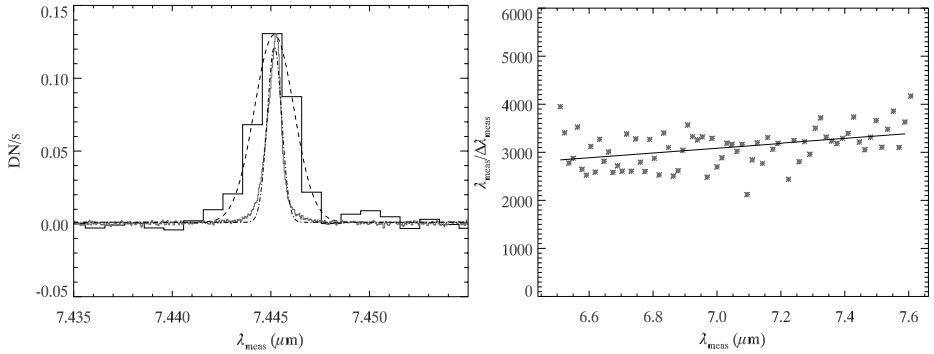

Figure 5.11 *Left*: One etalon line as seen by the MRS (solid black line) and by the high resolution measurements (solid grey line). The dotted lines are Gaussian fits to the data. *Right*: Resolving power R for the MRS subchannel 1C. The asterisks are the measured values at the line centroids, and the solid line is a linear fit to the data.

There is a spread in the measurement of the resolving power R of about 500. Insufficient S/N in the measurement of the etalon lines, which causes variations in the parameters of the Gaussian fits from line to line, may be part of the cause for this dispersion. In general, any source of noise in the original exposures can affect the shape of the lines, but we expect the flat-fielding to be the main source of error. Higher S/N again is desirable to achieve a narrower dispersion in the resolving power estimates. During FM testing, studies of the stability of the line shapes is essential to assess what is the magnitude of the variation in resolving power we should expect from one measurement to the other.

The etalon lines as measured by the MRS are the convolution of the intrinsic line shape

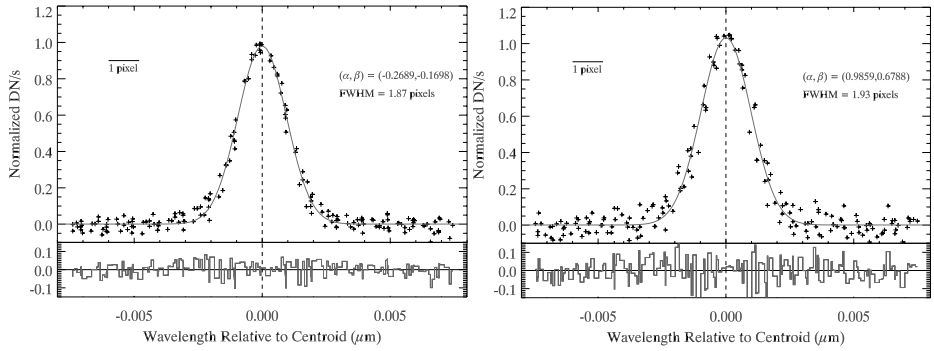

Figure 5.12 *Left:*: Overplotted etalon lines with their Gaussian centroids located at the origin, for position $(\alpha, \beta)= (-0.269, -0.170)$. The cross symbols correspond to the MRS data, while the solid grey line is a Gaussian fit to the resulting set of data. The residuals of the fit are shown at the bottom of the plot. The pixel size is also indicated. *Right*: Same as (a), but for position $(\alpha, \beta)= (0.986, 0.679)$

with the slit width of the spectrometer, which has a response that we can approximate by a Gaussian. For resolving power issues, we are more interested in getting the instrument's response unaffected by this convolution, and hence we want to deconvolve the measured profile with the intrinsic line shape. The derivation of the intrinsic line shape would require detailed modelling of the reflecting layers of the etalon device mounted on the MTS. Instead, we use the high resolution measurement of the etalon lines as a good approximation of the intrinsic line shape. Fig. 5.12 shows the Gaussian fits to the unresolved etalon line measured by MRS and the fit to the high resolution measurement for the same line. The theory of convolution of Gaussians states that the widths of two convolved Gaussian add in quadrature: $\sigma^2_{\text{convol}} = \sigma^2_1 + \sigma^2_2$

From the two measurements we obtain with our Gaussian fits and the expression above, we obtain an estimation of the line width, once it has been deconvolved with the intrinsic shape. We find that the deconvolved widths are about 10% smaller as compared with the MRS measurements. Since the width of the Gaussian is proportional to the resolution element, this decrease in the width translates to an equivalent increase of the resolving power. This increment brings us above our goal of $R > 3000$ at these wavelengths.

Line shape

Perhaps more important than an absolute wavelength calibration at this point, the study of the unresolved line shapes across the FOV is crucial. If the line is not symmetric, future dynamical studies using spectral lines might be affected by a purely instrumental effect. For instance, near the edge of the detector, internal reflections might cause additional line peaks or bumps. It is difficult to judge the symmetry of the etalon lines given the level of

pixel sampling we have in the data. With FWHMs of between 2 and 3 pixels, the lines might appear asymmetric, but they hardly provide a definitive answer.

In Fig. 5.12 we have overplotted 12 normalized neighboring etalon lines with wavelengths near 7.4μm with their Gaussian centroids all located at the origin, for two different positions of the FOV. The plots show a statistical line shape that is well fitted by a Gaussian, within the errors shown in at the bottom of the plots. For both positions, the FWHM of the fitted Gaussians is of about 1.9 pixels.

As mentioned before, undersampling reduces the accuracy with which the line centroids can be determined. Although geometrical ray tracing predicted line widths of less than one pixel, our measurements in Fig. 5.12 show that the actual line widths are close to Nyquist sampling, at least in the wavelength range studied here.

5.5 Summary and outlook

We have studied the wavelength properties of the MIRI Medium Resolution Spectrometer. Using input from optical modelling and an analysis of the synthetic etalon lines produced with the telescope simulator, we have designed a tool to obtain a wavelength calibration from MIRI test data. The wavelength calibration of the instrument before launch is of crucial importance for the development of the reduction software and for the planning of commissioning and science observations that will require the spectroscopic capabilities of JWST.

Even though we were restricted by the quality of the data, which we expect to improve during the testing of the Flight Model of MIRI, the different methods seem to provide the necessary accuracy to verify the instrument requirements. In particular, even at a moderate S/N ratio of about 15, the etalon line analysis provides wavelength references with an accuracy below a tenth of the resolution element. An absolute wavelength calibration will require smaller uncertainties in the determination of an absolute reference using the LWP filter. But even with our S/N restrictions, the effect of a wrong matching of the etalon lines with their actual wavelengths is not bigger than the separation between two etalon lines, and this should be improved with FM data. Fringing provides an interesting way of checking the results, but it might be more useful to study variations in the detector properties such as substrate thickness. The resolution-limited line shapes are well fitted by Gaussians and have FWHM larger than one pixel, minimizing the effect of a wrong calibration due to undersampling.

The analysis has been carried out for channel 1C of the detector, where we can establish an absolute reference with the LWP filter cutoff wavelength. However, this method can be extended to other channels by finding an absolute reference for those channels where a filter cutoff is not available. This reference can be, for example, the pattern created by synthetic lines from different etalon filters that overlap in some portions of the different subchannels. In this way, once we have obtained a full set of data with the FM, an absolute wavelength calibration can be achieved for the full wavelength range of MIRI.

ACKNOWLEDGEMENTS

This chapter would not have been possible without the input from many people within the MIRI European Consortium and in particular the MIRI test team. Our colleagues in the US have also provided very helpful comments and new ideas. In particular, this work would not have been possible without the Data Handling and Analysis Software (DHAS), developed by Jane Morrison, at the University of Arizona.